POLITECNICO DI TORINO
Repository ISTITUZIONALE

Numerical analysis and reduced-order modeling of a clustered aerospike engine

Original
Numerical analysis and reduced-order modeling of a clustered aerospike engine / Tozzi, D., Bach, C., Ferrero, A., Masseni, F., Pastrone, D.. - (2025). (EUCASS 2025 Rome (ITA) 30 June - 4 July 2025) [10.13009/EUCASS2025-388].

Availability:
This version is available at: 11583/3016856 since: 2026-10-21T11:45:36Z

Publisher:
EUCASS

Published
DOI:10.13009/EUCASS2025-388

Terms of use:

This article is made available under terms and conditions as specified in the corresponding bibliographic description in the repository

Publisher copyright

(Article begins on next page)

26 October 2026

DOI: 10.13009/EUCASS2025-388
11TH EUROPEAN CONFERENCE FOR AERONAUTICS AND SPACE SCIENCES (EUCASS)

Numerical Analysis and Reduced-Order Modeling of a Clustered Aerospike Engine

Daniele Tozzi⋆†, *Christian Bach*⋆⋆, *Andrea Ferrero*⋆, *Filippo Masseni*⋆ *and Dario Pastrone*⋆
⋆*Department of Mechanical and Aerospace Engineering, Politecnico di Torino*
Corso Duca degli Abruzzi 24, 10129 Turin, Italy
⋆⋆*Institute of Aerospace Engineering, Technische Universität Dresden*
Marschnerstrasse 32, 01307 Dresden, Germany
daniele.tozzi@polito.it · christian.bach1@tu-dresden.de · andrea_ferrero@polito.it ·
filippo.masseni@polito.it · dario.pastrone@polito.it
†Corresponding author

Abstract

The last decade has seen a growing interest in reusable launchers. The clustered aerospike engine consists of multiple thrusters, referred to as cells in the following, arranged in an annular fashion around a central aerospike nozzle. This technology appears particularly promising for reusable launch vehicles due to its continuous altitude adaptation and differential throttling capabilities. These features can be in principle exploited twice, during both the ascent and landing phases of flight. In this context, accurately predicting engine performance while maintaining low computational effort is challenging, especially considering the complex and non-linear plume interactions that arise during differential throttling operation. In this paper, a procedure to generate a non-linear reduced-order model of a clustered aerospike engine has been implemented. This model is capable of predicting, with an error below 10 % for most test cases analyzed, axial and lateral components of thrust in different configurations. A CFD analysis has been carried out, considering a 28-cells aerospike scale model in a cold-flow configuration. Different RANS simulations were performed, aiming for a good compromise between accuracy and computational cost, to construct two different databases. The training database consists of 14 simulations with two active cells at different angular distances, plus one simulation with a single active cell. From this dataset, plume interactions were analyzed and characterized through the definition of appropriate interaction coefficients. Using these coefficients, a reduced-order model of the aerospike has been proposed and subsequently validated against a testing database, that instead comprises various symmetrical and asymmetrical configurations with a larger number of active cells. The proposed reduced-order modeling procedure is formulated in such a way that, in principle, it could be applied to any arbitrary aerospike engine and, at least for axial thrust predictions, even in a scenario where only experimental data would be available. Furthermore, this model could be applied as a first-order approximation to predict thrust components and their variations in the event of random failure modes, where one or more cells may become inactive during flight. The proposed model demonstrates good accuracy in predicting axial thrust, while further refinement together with a larger testing database is needed to improve its predictions of lateral loads.

1 Introduction

In recent years, there has been a growing commercial interest in the development of Reusable Launch Vehicles (RLVs). One of the primary challenges faced by these reusable systems is the need for adaptable and efficient propulsion technologies. The well-known and traditionally employed bell nozzles are significantly limited in performance in two ways. Firstly, the possible occurrence of flow separation and the related undesirable side-load activity at sea level severely limits the choice of expansion ratio (ϵ) to lower values, leading to reduced performance.[1] Secondly, a fixed expansion ratio implies that, during most of the flight, the engine operates under sub-optimal conditions, which can result in losses of up to 15% of the theoretical performance of a perfectly adapted nozzle.[2] These limitations are even more critical in RLVs, where inefficiencies affect both the ascent and landing phases of flight. Additionally, there are further challenges associated with the use of traditional bell nozzles in retro-propulsion applications.[3]

In an aerospike or plug nozzle, the direct contact of the expanding jet with the surrounding air enables it to overcome these disadvantages, as the flow is able to continuously adapt to the changing external pressure.[4] The

Copyright © 2025 by the present authors. Published by the EUCASS association with permission.

DOI: 10.13009/EUCASS2025-388

renewed interest in this type of advanced nozzle is therefore unsurprising, as in recent years the aerospike nozzle has been the focus of numerous research efforts in both industry and academia.[5]

Despite its attractive characteristics, such as altitude adaptation, compact form factor, and higher achievable expansion ratios, the plug nozzle also presents several limitations, mainly related to manufacturing and cooling challenges.[6] The clustered version of the aerospike nozzle, which consists of multiple thrusters (referred to as cells in the following) arranged around a central plug, can help alleviate the severe heat loads that occur at the throat of a single-chamber annular architecture, while also enabling differential throttling operation thanks to the separate thrust chambers. The main disadvantage of this configuration lies in the complex non-linear interactions and related aerodynamic losses that arise from the different plumes interacting on the plug surface. Some analytical and theoretical work has been carried out to characterize these intricate flowfields and to estimate the losses associated with the finite number of modules.[7–10]

In this context, the present work aims to define a purely mathematical procedure to construct a reduced-order model capable of predicting thrust in different working configurations (i.e., varying number and position of active cells) for an arbitrary aerospike engine. Starting from a set of Reynolds-Averaged Navier-Stokes (RANS) cold-flow simulations composing the training database, appropriate interaction coefficients are introduced to account for the non-linear interactions of plumes from cells at different angular distances. The model is then mathematically formulated and validated against a separate testing database, which includes both cyclically symmetric and non-symmetric configurations, to assess its capability to predict the axial and lateral components of thrust.

The model is structured such that, at least for axial thrust predictions, it could also be constructed using a dataset obtained from a hypothetical experimental campaign.

2 The aerospike model

The aerospike model used for the simulations is similar to the one developed during the Master's thesis research project of Mulas.[11] It consists of a sub-scale 28-cell cluster of bell-type modules with a truncated annular plug (see Figure 1b). A schematic of the cross-section of a module is shown in Figure 1a, while the exact geometric parameters are listed in Table 1.

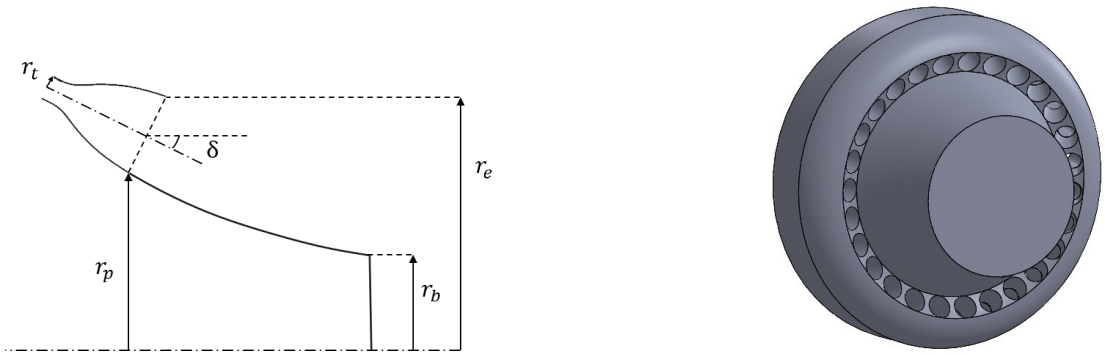

(a) Cross section of the plug and a single module

(b) 3-D view of the complete CAD model

Figure 1: Aerospike geometry schematics

The main goal of the thesis work was to compare the performance of a clustered aerospike engine and a state-of-the-art octaweb configuration in retro-propulsion applications. The test case used for this comparison was derived from the subsonic landing burn of the RETALT1 mission by Deutsches Zentrum für Luft-und Raumfahrt (DLR).[12] Regarding the aerospike nozzle design specifically, the plug contour was developed following the procedure outlined by Lee,[13] while the internal nozzle of each module was designed at Technische Universität Dresden (TUD) as a Thrust Optimized Contour (TOC), using an internal tool. Since the design of the entire clustered aerospike resulted from a complex analysis aimed at enabling a meaningful comparison with the octaweb configuration, the design process was not straightforward. For interested readers, further details can be found in Mulas' thesis.[11]

In the present work, the aerospike nozzle was simulated under cold-flow conditions at a Nozzle Pressure Ratio

DOI: 10.13009/EUCASS2025-388

(NPR) of 10, defined as:

$$NPR = \frac{p_c^o}{p_a} \tag{1}$$

where p_c^o is the total chamber absolute pressure, and p_a is the ambient absolute pressure.

Table 1: Geometric parameters of the clustered aerospike (see Figure 1)

Geometric parameters	
Module nozzle ϵ_N	2.48
Nozzle inclination δ	25.6°
Throat radius r_t	2.39 mm
External radius r_e	43.67 mm
Plug max radius r_p	36.87 mm
Base radius r_b	22.55 mm

3 Simulations database

The simulations were carried out using the Ansys Fluent software.[14] Symmetries were exploited where possible to reduce computational cost and speed up the creation of the datasets.

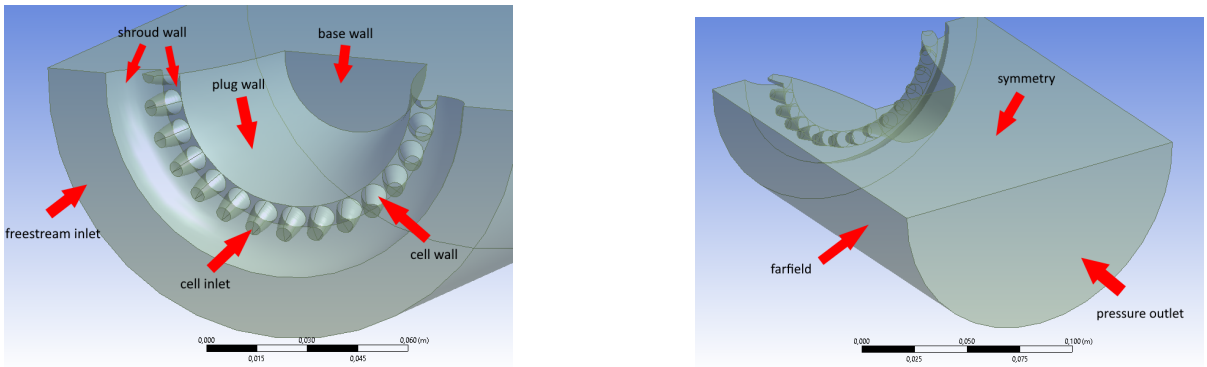

Figure 2: Numerical domain and boundary conditions

3.1 Geometry

The numerical domain is shown in Figure 2, along with the different applied boundary conditions. Although various aerospike configurations were simulated, the domain extension (see Figure 3) remained unchanged. In all cases, an unstructured mesh of polyhedral cells was defined, with an inflation layer applied to the plug and internal cell walls to achieve $y^+ \lesssim 1$ for all simulations. Regarding the grid size, a balance was sought between accuracy and computational cost, given the large number of simulations required to construct the datasets. Since detailed flowfield analysis around the plug was not the primary objective, only the convergence of force values was monitored to determine the final mesh size. The main motivation behind this work is to develop a procedure that enables the definition and calibration of a non-linear reduced-order model trained on reference data. For this reason, the focus is placed on the development of the reduced-order model, rather than on the accuracy of the reference database, which can eventually be replaced by experimental data or high-fidelity simulations.

3.2 Physical model

The full 3-D RANS equations were discretized and solved in Ansys Fluent.[14] Dry air was chosen as the working fluid (constant specific heats ratio $\gamma = 1.4$), modeled as an ideal gas with the Sutherland law for dynamic viscosity. The SST k-ω two-equation turbulence closure model[15] was selected, as it has demonstrated good accuracy in compressible nozzle flow simulations.[16] Regarding the boundary conditions, the total pressure at the freestream pressure inlet was set to the ambient value of $p_a = 50$ kPa, along with a total temperature of 300 K. The same static pressure was specified

DOI: 10.13009/EUCASS2025-388

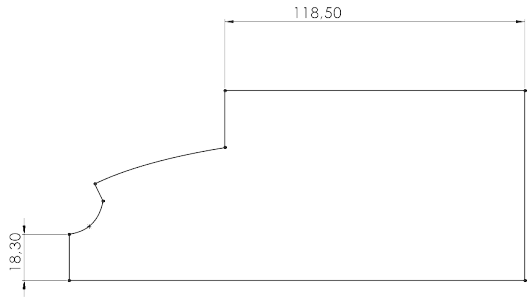

Figure 3: Geometric extension of the computational domain in [mm]

at the pressure outlet and the farfield. At the farfield boundary, a very small Mach number was also prescribed. As for the cell inlets, located exactly at the throats of the modules, a total pressure of $p_c^o = 500$ kPa and a static pressure of 264.14 kPa were prescribed, corresponding to a unit isentropic Mach number. The total temperature at the inlets was also set to 300 K. Inoperative cells were simply closed off by setting the corresponding inlets as no-slip walls.

These values of pressures and temperatures were selected to be representative of a sub-scale cold-flow testing campaign that could potentially be carried out at the TUD facilities. In fact, the aerospike design was originally developed with the possibility of such an experimental campaign in mind.

3.3 Solver

A density-based implicit solver was employed for all simulations. For spatial discretization, a second-order upwind scheme was used for both the flow equations and turbulence transport, with a Roe Flux Difference Splitting scheme applied to the convective fluxes. Gradient reconstruction was performed using a least-squares cell-based method.

3.4 Training database

The training database from which the reduced-order model is defined consists of one simulation with a single active cell and 14 simulations with two active cells, covering all possible angular distances $\Delta\theta$ ranging from $360°/28 = 12.857°$ to $180°$. Figure 4 shows the reference frame adopted for the calculations.

We begin with the single active cell simulation by first calculating the axial and radial force contributions of the individual module. The stream force at the cell inlet was computed as:

$$\boldsymbol{SF} = \int_A \left[\rho(\boldsymbol{u}\cdot\boldsymbol{n})\boldsymbol{u} + (p - p_a)\boldsymbol{n}\right]\, dA \tag{2}$$

where $\boldsymbol{n}$ is the unit normal vector at the cell inlet surface.

Next, the force contribution from the nozzle internal wall was calculated by integrating both pressure and viscous components:

$$\boldsymbol{F_{cn}} = \int_A \left[-(p - p_a)\boldsymbol{n} + \boldsymbol{\tau}\cdot\boldsymbol{n}\right] dA \tag{3}$$

Where $\boldsymbol{\tau}$ is the viscous stress tensor. By projecting along the x-direction, the total *axial* thrust contribution of the single module was found to be:

$$F_{cell,x} = SF_x + F_{cn,x} = 10.141 \text{ N} \tag{4}$$

Similarly, the *radial* cell force contribution was computed as:

$$F_{cell,r} = SF_r + F_{cn,r} = 4.861 \text{ N} \tag{5}$$

DOI: 10.13009/EUCASS2025-388

These two values will naturally remain constant for all cells in every case, regardless of the specific aerospike configuration.

The plug and base force contributions were also computed by integrating both pressure and viscous stresses along the surface. For the single active cell, we obtained:

$$F_{1,x} = -0.720 \text{ N} \tag{6}$$

and:

$$F_{1,r} = 2.091 \text{ N} \tag{7}$$

For the remaining simulations in the training database, some additional considerations regarding lateral loads need to be made. As shown in Figure 4, due to the symmetry of the two-active-cell configurations, the lateral force from the plug is always directed along the z-direction. To simplify the definition of the reduced-order model for side force prediction, we assumed that the jets from the modules produce only a radial force component along the plug.

With this assumption and referencing Figure 4, the values of $F_{pb,r}$ were extracted from Fluent and are reported in Table 2. It is worth noting that in the case of experimental data, where only the component $F_{pb,z}$ might be measurable, this radial force could still be estimated as:

$$F_{pb,r} = \frac{F_{pb,z}}{2\cos(\theta/2)} \tag{8}$$

Table 2: Plug and base axial and radial forces as a function of angular distance between the two active cells. The radial forces refer to the contribution of the single cell of each couple (see Figure 4)

$\Delta\theta$ [°]	$F_{pb,x}$ [N]	$F_{pb,r}$ [N]
12.857	-0.880	2.543
25.714	-0.176	2.842
38.571	-0.716	2.631
51.428	-1.142	2.519
64.285	-2.018	2.296
77.142	-2.280	2.200
90.000	-2.478	2.085
102.856	-2.878	2.073
115.713	-3.682	2.014
128.570	-3.346	2.043
141.427	-3.510	1.991
154.284	-3.868	2.005
167.141	-3.682	1.955
180.000	-3.592	1.984

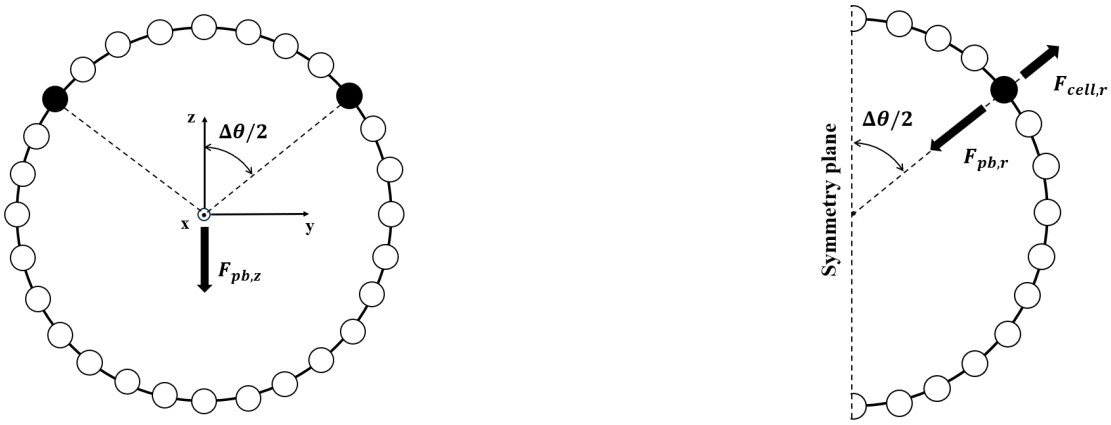

Figure 4: Adopted reference frame and schematic of the forces in the two-active-cell configurations

DOI: 10.13009/EUCASS2025-388

3.5 Testing database

The testing database is needed only to validate the model, and consists of both cyclically symmetric and non-symmetric configurations. The symmetric simulations include the following cases:

- N = 4 active cells, one every 90°;
- N = 7 active cells, one every 51.428°;
- N = 14 active cells, one every 25.714°;
- N = 28, i.e., all cells active.

Given the cyclical symmetry, no side loads act on the aerospike in these configurations. The axial thrust contributions of the plug and base for these four cases are reported in Table 3, and are shown in Figure 5 along with the two-active-cell configuration at $\Delta\theta$ = 180° (which is also cyclically symmetric). Here, the strong non-linear behavior arising from plume interactions is clearly observable and must be accurately captured by the reduced-order model.

Table 3: Axial forces acting on the plug and base of the cyclically symmetric configurations

N	$\Delta\theta$ [°]	$F_{pb,x}$ [N]
4	90.000	-5.816
7	51.428	-5.033
14	25.714	-1.834
28	12.857	8.624

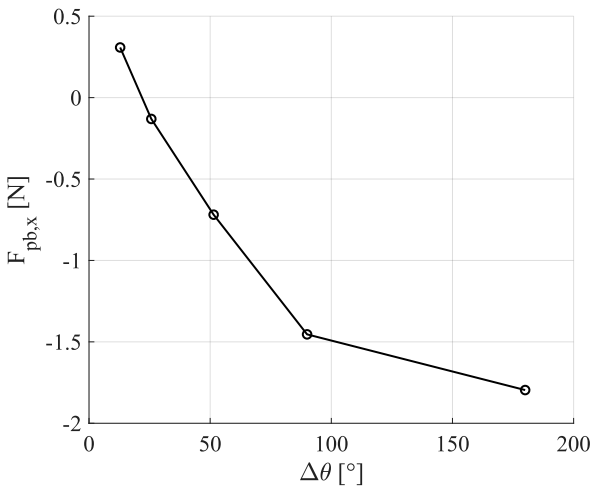

Figure 5: Axial forces from plug and base of all cyclically symmetric configurations

The non-symmetric part of the testing database consists of:

- 1 simulation with 27 active cells;
- 2 simulations with 26 active cells;
- 3 simulations with 25 active cells;
- 3 simulations with 23 active cells;
- 1 simulation with 19 active cells.

The exact configurations are illustrated in Figure 6. Note that, to reduce computational cost for the construction of the testing database, all of these simulations retained a single symmetry plane, despite not exhibiting perfect cyclical symmetry. In Table 4, both the axial and lateral plug and base forces are reported for this portion of the testing database (always refer to Figure 4 for the coordinate system).

DOI: 10.13009/EUCASS2025-388

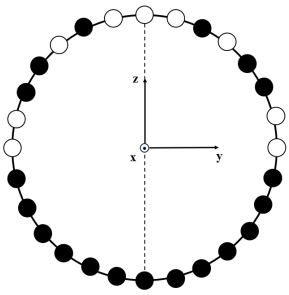

(a) $N = 19$

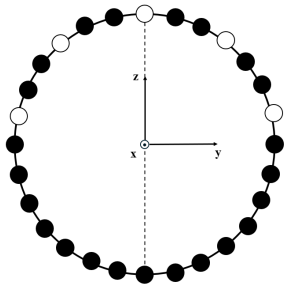

(b) $N = 23$

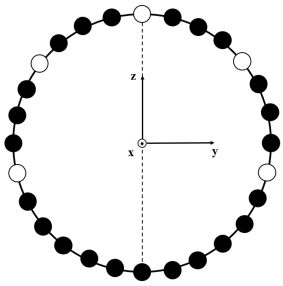

(c) $N = 23$

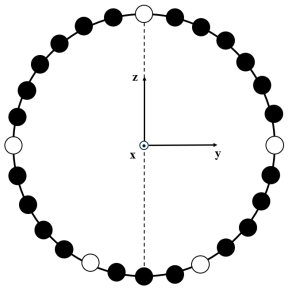

(d) $N = 23$

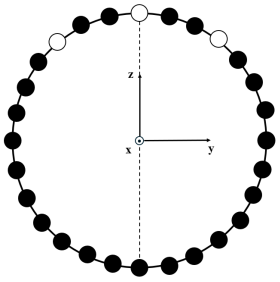

(e) $N = 25$

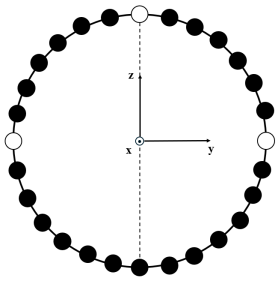

(f) $N = 25$

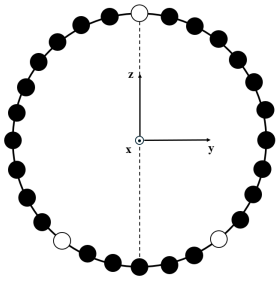

(g) $N = 25$

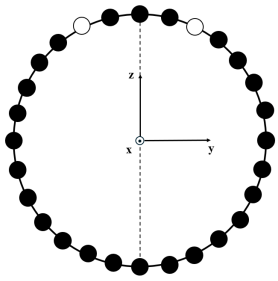

(h) $N = 26$

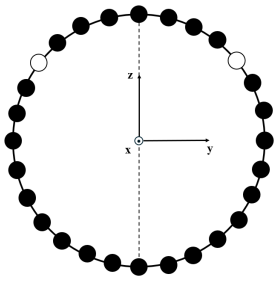

(i) $N = 26$

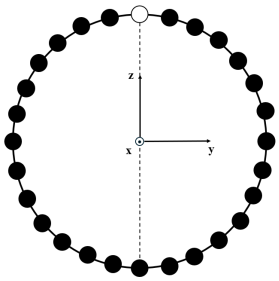

(j) $N = 27$

Figure 6: Non-ciclically symmetric configurations of the testing database (see Table 4 for the force values), inactive cell positions highlighted in white

DOI: 10.13009/EUCASS2025-388

Table 4: Axial and lateral forces of the non-cyclically symmetric part of the testing database, acting on the plug and base of the aerospike

N	$F_{pb,x}$ [N]	$F_{pb,z}$ [N]
27	8.624	2.366
26 (Fig. 6i)	8.000	4.524
26 (Fig. 6h)	5.698	2.990
25 (Fig. 6g)	4.754	6.234
25 (Fig. 6f)	4.830	2.366
25 (Fig. 6e)	4.845	-1.388
23 (Fig. 6d)	3.135	7.338
23 (Fig. 6c)	3.297	4.644
23 (Fig. 6b)	3.229	-2.128
19	-3.186	14.074

4 Reduced-order modeling procedure

We can now define the exact reduced-order modeling procedure. The model takes as input an arbitrary configuration with a given number of active cells $N > 1$, and outputs a prediction of the axial and lateral forces acting on the aerospike nozzle.

4.1 Axial thrust model

4.1.1 Linear models

The simplest model one can consider is linear, based on the single active cell configuration. The axial thrust is then given by:

$$F_{linear1,x} = N\left(F_{cell,x} + F_{1,x}\right) \tag{9}$$

An alternative is to use one twenty-eighth of the axial force from the configuration with all active cells to define another linear model:

$$F_{linear2,x} = N\left(F_{cell,x} + \frac{F_{28,x}}{28}\right) \tag{10}$$

We will refer to these two models as *linear 1* and *linear 2* respectively. They will be used as a baseline to compare the results of the proposed model.

4.1.2 Proposed model

Using the 14 two-active-cell simulations from the training database, we define a set of *axial interaction coefficients* as:

$$c_x^i(\Delta\theta) = \frac{F^i_{pb,x}}{2F_{1,x}}\,, \quad i = 1, \ldots, 14 \tag{11}$$

These coefficients are functions of the angular distance between two active cells, $\Delta\theta$, and represent the only part of the reduced-order model that accounts for plume interaction non-linearities. They are plotted in Figure 7.

We can express the axial force prediction of the model as:

$$F_{model,x} = N \times F_{cell,x} + F^{tot}_{pb,x} \tag{12}$$

where $F^{tot}_{pb,x}$ is the thrust contribution from the plug and base. We can then compute the contribution of the j-th active cell to the plug and base force as:

$$F^j_{pb,x} = \sum_{\substack{i=j-1 \\ i\neq j}}^{j+1} \frac{c_x^i \times F_{1,x}}{N_{adj}} \tag{13}$$

where N_{adj} is the number of adjacent active cells, which is always equal to 2, except in the case of only two active cells. This means that, in practice, for the j-th active cell, only the interactions with its two nearest neighbors, $j-1$ and $j+1$,

DOI: 10.13009/EUCASS2025-388

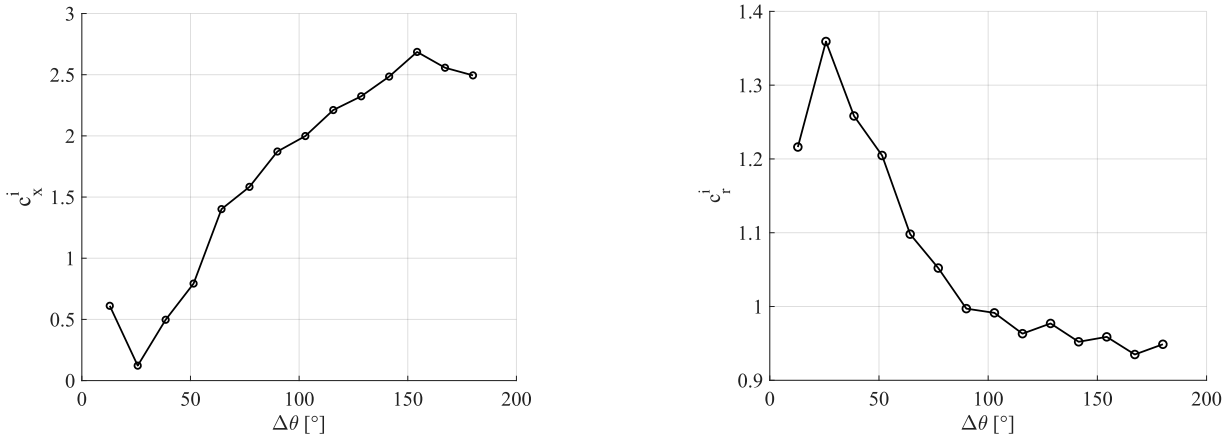

(a) Axial coefficients

(b) Radial coefficients

Figure 7: Interaction coefficients of the proposed model

are considered. Now, it is possible to express the model's axial force prediction as:

$$F_{model,x} = N \times F_{cell,x} + \sum_{j=1}^{N} \left(F_{pb,x}^{j} \right) = N \times F_{cell,x} + \sum_{j=1}^{N} \left(F_{1,x} \sum_{\substack{i=j-1 \\ i \neq j}}^{j+1} \frac{c_x^i}{N_{adj}} \right) \tag{14}$$

It is straightforward to verify that the model returns the exact force value when $N = 2$ and $N_{adj} = 1$. In the case of a hypothetical experimental campaign, where only the combined values of $F_{cell,x} + F_{1,x}$ and $2F_{cell,x} + F_{pb,x}^{i}$ would be available as single data points, we would simply need to re-define the interaction coefficients as:

$$c_x^i(\Delta\theta) = \frac{F_{pb,x}^{i} + 2F_{cell,x}}{2(F_{1,x} + F_{cell,x})} \tag{15}$$

Then the model would be expressed as:

$$F_{model,x} = \sum_{j=1}^{N} \left[\sum_{\substack{i=j-1 \\ i \neq j}}^{j+1} \frac{c_x^i \times (F_{1,x} + F_{cell,x})}{N_{adj}} \right] \tag{16}$$

It can be shown analytically that this new definition is exactly equivalent to the one shown in equation (14).

4.2 Lateral force models

4.2.1 Linear models

For the lateral force models, the approach is very similar to the axial case. However, it is now necessary to account for the fact that the individual force contributions are vector quantities. By defining a unit radial vector $\boldsymbol{r}^j$ corresponding to the j-th active cell (see Figure 8), it is straightforward to extend the linear model for lateral load prediction:

$$\boldsymbol{F}_{\boldsymbol{linear,r}} = \sum_{j=1}^{N} \left(-F_{cell,r} \boldsymbol{r}^j + F_{1,r} \boldsymbol{r}^j \right) \tag{17}$$

Naturally, only one linear model can be defined now, since no lateral force acts on the $N = 28$ configuration.

4.2.2 Proposed model

Similarly to the axial case, we define the *radial interaction coefficients* as:

$$c_r^i(\Delta\theta) = \frac{F_{pb,r}^{i}}{2F_{1,r}}, \quad i = 1, \ldots, 14 \tag{18}$$

DOI: 10.13009/EUCASS2025-388

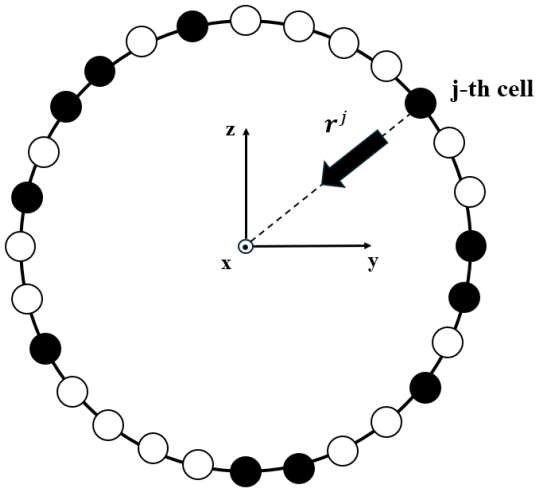

Figure 8: Radial unit vector for the j-th active cell

These coefficients are shown in Figure 7. Using the previously defined $\boldsymbol{r}^j$, we now express the (vectorial) plug and base contribution of the j-th cell as:

$$\boldsymbol{F}_{\boldsymbol{pb,r}}{}^j = \sum_{\substack{i=j-1 \\ i\neq j}}^{j+1} \frac{c_r^i \times F_{1,r}}{N_{adj}} \boldsymbol{r}^i \tag{19}$$

The total lateral force is then computed by summing the plug and cell (vectorial) contributions:

$$\boldsymbol{F}_{\boldsymbol{model,r}} = \sum_{j=1}^{N} \left(-F_{cell,r}\boldsymbol{r}^j + \boldsymbol{F}_{\boldsymbol{pb,r}}{}^j\right) = \sum_{j=1}^{N} \left[-F_{cell,r}\boldsymbol{r}^j + \sum_{\substack{i=j-1 \\ i\neq j}}^{j+1} \frac{c_r^i \times F_{1,r}}{N_{adj}} \boldsymbol{r}^i\right] \tag{20}$$

By constructing the model in this way, we ensure that every cyclically symmetric configuration yields an exact prediction of zero side loads.

5 Results

The previously described reduced-order models were validated against the symmetric and non-symmetric configurations comprising the testing database.

5.1 Axial thrust predictions

Figure 9 presents the results for the cyclically symmetric configurations. The error shown in the figure is defined as:

$$\text{err } [\%] = \frac{\|F_{model} - F_{exact}\|}{\|F_{exact}\|} \times 100 \tag{21}$$

As for the predictions on the non-cyclically symmetric part of the database, they are listed in Table 5. The proposed model outperforms the linear model based on the single-active-cell configuration (*linear 1*) in virtually all cases. As for the other linear model, it performs better when the number of active cells is relatively high (i.e., $N > 19$), as could have been expected. However, when the number of active modules is lower, as in some of the cyclically symmetric cases (see Figure 9), this second linear model tends to significantly overestimate thrust. Overall, the proposed model's error remains well below 10% in most cases, which can be considered a satisfactory result for such a simple model.

5.2 Lateral load predictions

In the case of lateral loads, the nature of the testing database must be carefully considered. As previously mentioned, due to time and computational cost constraints, all testing simulations retained a single plane of symmetry (as can

DOI: 10.13009/EUCASS2025-388

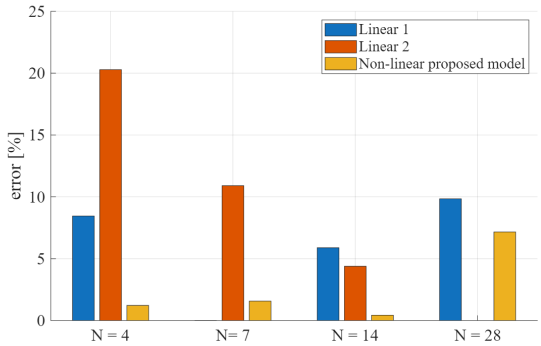

Figure 9: Axial thrust errors on the cyclically symmetric part of the testing database

Table 5: Errors on the axial thrust for the non-cyclically symmetric part of the testing database

N	$err_{nonlin\ mod}$ [%]	err_{lin1} [%]	err_{lin2} [%]
27	6.930	9.738	0.112
26 (Fig. 6i)	6.897	9.837	0.003
26 (Fig. 6h)	6.102	9.066	0.858
25 (Fig. 6g)	5.691	8.811	1.141
25 (Fig. 6f)	5.719	8.838	1.111
25 (Fig. 6e)	5.725	8.843	1.105
23 (Fig. 6d)	4.863	8.333	1.671
23 (Fig. 6c)	4.929	8.396	1.601
23 (Fig. 6b)	4.901	8.369	1.630
19	2.342	5.538	4.770

observed in Figure 6). Therefore, although the model outputs are vector quantities, the direction of the force will always be correct (see Figure 10), due to this symmetry and how the reduced-order models were defined. Given this, we can simply analyze the errors on the predicted force magnitude, which are listed in Table 6. It can be observed that the proposed model outperforms the linear one across all testing database, with errors below 10% in most cases.

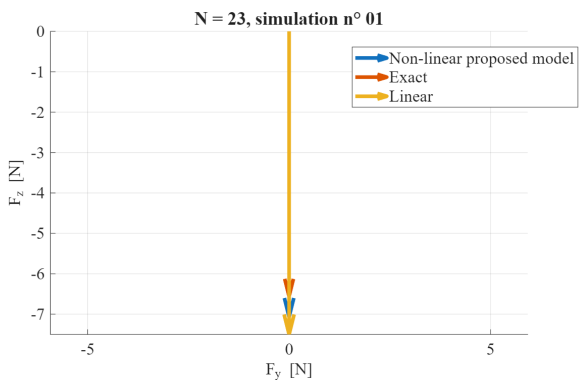

Figure 10: Example case (see Figure 6b) showing the exact and predicted lateral force vectors

DOI: 10.13009/EUCASS2025-388

Table 6: Errors on the lateral force magnitude for the non-cyclically symmetric part of the testing database

N	$\text{err}_{nonlin\ mod}$ [%]	err_{lin} [%]
27	4.589	11.022
26 (Fig. 6i)	11.004	17.834
26 (Fig. 6h)	5.914	12.431
25 (Fig. 6g)	7.405	14.012
25 (Fig. 6f)	4.561	10.995
25 (Fig. 6e)	8.857	15.546
23 (Fig. 6d)	7.730	14.357
23 (Fig. 6c)	14.245	21.274
23 (Fig. 6b)	18.264	25.532
19	19.109	36.940

6 Conclusions

In this paper, a simple engineering procedure to generate a reduced-order model for an arbitrary clustered aerospike engine has been defined. This model is capable of predicting thrust and lateral forces acting on the nozzle, given a configuration with a specified number and arrangement of active cells. Two databases of cold-flow CFD simulations were constructed using the Ansys Fluent software. The proposed model was then built from a training dataset of 15 simulations and subsequently validated against a different testing database. These results were further compared with simpler linear models.

When predicting axial thrust levels, the proposed model seems to show good performance, achieving errors below 10% in all tested configurations. However, in cases where the number of active cells is high ($N > 19$ for the test cases analyzed), the linear model based on the all-cells-active simulation outperforms the proposed one.

As for lateral load predictions, the proposed model consistently outperforms the linear one, although the associated errors are generally higher. It is important to note that these results refer only to errors in lateral force magnitude and must therefore be interpreted with caution: while the model was able to predict the correct force direction, this was most certainly due to the symmetric nature of the testing database. If the model were applied to fully non-symmetric test cases, the error would likely propagate to the predicted force direction as well. Moreover, the presented model was constructed and tested at only one value of NPR. Moving away from this specific operating point could significantly affect the model's performance, especially in the presence of wake-closure phenomena, which are expected to influence the non-linear plume interactions.

Given these limitations, alternative approaches to reduced-order modeling for side-load prediction should be investigated. Additionally, expanding the testing database to include fully non-symmetric simulations, as well as configurations with fewer active cells, would provide a more comprehensive evaluation of the proposed model's predictive capabilities. A new axial thrust model that blends the linear and non-linear formulations based on the number of active cells will also be explored in future work.

7 Acknowledgments

Computational resources were provided by HPC@POLITO, a project of Academic Computing within the Department of Control and Computer Engineering at the Politecnico di Torino (http://www.hpc.polito.it).

DOI: 10.13009/EUCASS2025-388

References

[1] J. Östlund. Flow processes in rocket engine nozzles with focus on flow separation and side-loads. Technical report, KTH Royal Institute of Technology, 2002.

[2] G. Hagemann, H. Immich, T. van Nguyen, and G. E. Dumnov. Advanced rocket nozzles. *Journal of Propulsion and Power*, 14:620–634, 1998.

[3] G. Scarlatella, M. Tajmar, and C. Bach. Advanced nozzle concepts in retro-propulsion applications for reusable launch vehicle recovery: a case study. In *72nd International Astronautical Congress (IAC)*, 2021.

[4] J. H. Ruf and P. K. McConnaughey. The plume physics behind aerospike nozzle altitude compensation and slipstream effect. In *33rd Joint Propulsion Conference and Exhibit*, 1997.

[5] C. Bach, S. Schöngarth, B. Bust, M. Propst, J. Sieder-Katzmann, and M. Tajmar. How to steer an aerospike. In *69th International Astronautical Congress (IAC)*, 2018.

[6] C. Bach, J. Sieder-Katzmann, M. Propst, M. Tajmar, and J. Sieder-Katzmann. Evaluation of the performance potential of aerodynamically thrust vectored aerospike nozzles. In *67th International Astronautical Congress (IAC)*, 2016.

[7] T. Tomita, M. Takahashi, and H. Tamura. Flow field of clustered plug nozzles. In *33rd Joint Propulsion Conference and Exhibit*. American Institute of Aeronautics and Astronautics Inc, AIAA, 1997.

[8] F. Nasuti and M. Onofri. Theoretical analysis and engineering modeling of flowfields in clustered module plug nozzles. *Journal of Propulsion and Power*, 15:544–551, 1999.

[9] M. Fick and R. H. Schmucke. Performance aspects of plug cluster nozzles. *Journal of Spacecraft and Rockets*, 33:507–512, 1996.

[10] T. Ito and K. Fujii. Flow field and performance analysis of aerospike nozzles with simplified clustered modules. *Transactions of the Japan Society for Aeronautical and Space Sciences*, 47:17–22, 2004.

[11] A. Mulas. Comparison of octaweb configuration and annular aerospike nozzle for reusable launch vehicles: design and experimental set-up commissioning. Master's thesis, Politecnico di Torino, 2023.

[12] Ali Gülhan, Ansgar Marwege, and Jan Vos. Retro propulsion assisted landing technologies: the retalt project, 7 2022.

[13] C. C. Lee. Fortran programs for plug nozzle design. Technical report, Brown Engineering Company, Inc., 1963.

[14] Ansys, Inc., Canonsburg, PA. *ANSYS Fluent User's Guide*, 2023. Release 2023 R2.

[15] F. R. Menter. Zonal two equation k-ω turbulence models for aerodynamic flows. In *24th Fluid Dynamics Conference*. AIAA, 7 1993.

[16] C. Tian and Y. Lu. Turbulence models of separated flow in shock wave thrust vector nozzle. *Engineering Applications of Computational Fluid Mechanics*, 7:182–192, 2013.